Rakenteiden Mekaniikka (Journal of Structural Mechanics)
Vol. 56, No. 1, 2023, pp. 1–23
http://rakenteidenmekaniikka.journal.fi
https://doi.org/10.23998/rm.119608

VERTAISARVIOITU
KOLLEGIALT GRANSKAD
PEER-REVIEWED
www.tsv.fi/tunnus

Four-node quadrilateral C^0-element based on cell-based smoothed strains strategy and third-order shear deformation theory for functionally graded carbon nanotube reinforced composite plates

Lan Hoang Ton-That

Summary This study indicates the analysis of functionally graded carbon nanotube reinforced composite (FG-CNTRC) plates using a four-node quadrilateral element related to the C^0-type of Reddy's third-order shear deformation theory (C^0 HSDT) and cell-based smoothed strains (CS) strategy. Reddy's theory is surely taking the advantages and desirable properties of the third-order shear deformation theory. Besides, FG-CNTRC plates with advanced material properties are changed from the bottom to top surface with four kinds of carbon nanotube (CNTs). Numerical results and comparison with other reference solutions suggest that the benefits of the present element are accuracy and efficiency in analysis of FG-CNTRC plates.

Keywords: C^0-type, HSDT, four-node quadrilateral element, cell-based smoothed strains, FG-CNTRC plate

Received: 26 May 2022. Accepted: 19 January 2023. Published online: 2 May 2023.

Introduction

In the past few decades, carbon nanotubes (CNTs) with their outstanding features have made a big step forward for materials science. They have some advantages related to their remarkable mechanical, thermal and electrical properties [1–7]. From the structural review, their material properties are listed as high strength, low density, stiffness, etc. And they become a good candidate for composite structures. For this reason, the behaviors of FG-CNTRC plates need to be studied particularly.

Beside developing and manufacturing novel advanced engineering materials, many theories have been introduced into analyses from thin to thick plates such as the classical plate theory (CPT), the first-order shear deformation theory (FSDT), the higher-order shear deformation theory (HSDT), the layer-wise theory (LWT) and variable kinematics models. The FSDT is often applied because of its simplicity and

low computational cost [8–10]. But we may easily recognize that the third-order shear deformation plate theories are the accurate theories and effective due to the quadratic variation of the transverse shear strains and stresses along the thickness of plate as well as the shear locking free [11]. On the other hand, numerical methods have been expanded for the analysis of composite structures as given by authors [12–20] and so on. Specifically, the free vibration analysis of functionally graded carbon nanotube reinforced composite (FG-CNTRC) conical shell was carried out by using element-free kp-Ritz method. Based on the first-order shear deformation shell theory, the approximate displacement field was expressed by the shape function of the nuclear particle as in reference of author Xiang [12]. Author Farzam and colleague [13] investigated the thermal and mechanical buckling analysis of functionally graded carbon nanotube reinforced composite (FG-CNTRC) plates by using isogeometric analysis (IGA) based on modified couple stress theory. Besides, a 3D EFG method based on the Strain-Rotation decomposition theorem was presented to investigate the nonlinear bending behavior of functionally graded carbon nanotube reinforced composite (FG-CNTRC) plates. Due to its overcoming the drawbacks of classical finite element methods, Strain-Rotation decomposition theorem provided a dependable theoretical support for the nonlinear analysis as follows author Zhou [14]. Moreover, an other analysis was presented for functionally graded carbon nanotube-reinforced composite (FG-CNTRC) plates using the element-free kp-Ritz method by Lei and partners [15]. By means of the variational differential quadrature (VDQ) method, author Ansari [16] analyzed the free vibration characteristics of embedded functionally graded carbon nanotube-reinforced composite (FG-CNTRC) spherical shells on Pasternak foundation. Furthermore, Chau-Dinh and partners [17] developed a new three-node triangular plate element to analyze laminated composite plates based on the higher-order shear deformation theory (HSDT). Originating from the MITC3+ element, the displacement fields based on the HSDT were calculated by simple linear functions of the triangular element with three nodes and a cubic supplemented function related to a node located at the centroid of this element. The shear strain fields in transverse direction were estimated according to the MITC3+ element. The in-plane strain fields were improved by edge-based smoothed (ES) strain method. A cell-based smoothed discrete shear gap method (CS-FEM-DSG3) using three-node triangular element was recently proposed for the static and free vibration analyses of carbon nanotube reinforced composite (CNTRC) plates by Truong-Thi and colleagues [18]. The CS-FEM-DSG3 element was enhanced from the original DSG3 element by using smoothing technique to modify the stiffness of the DSG3 element while it still received the locking-free speciality of the former. In the most basic way, author Zhu [19] presented bending and free vibration analyses of thin-to-moderately thick composite plates reinforced by single-walled carbon nanotubes using the finite element method based on the first order shear deformation plate theory. Mostafa [20] examined the free vibration characteristics of plates containing a cutout that were reinforced with uniform or nonuniform distribution of carbon nanotubes. The first-order shear deformation plate theory was used to estimate the kinematics of the plate and the solution method was based on the Ritz method with Chebyshev basis polynomials, etc.

Going back to FSDT with clear mentions, finite element formulation only requires C^0 continuous shape functions as well as the weak-form equations only require the first

derivative of displacement field. However, shear locking phenomenon occurs when the thickness-to-length ratio of plate gradually approaches zero and it can be handled using reduced integration. With the higher-order shear deformation theory (HSDT), we recognize that it is commonly used because it gives accurate transverse shear stresses as well as does not need shear correction factors. But with low-order finite elements such as four-node quadrilateral element, the requirement of C^1-continuous approximation for the displacement fields in the higher-order shear deformation theory causes some impediments. To overcome these shortcomings, the HSDT is revised form from C^1 to C^0 continuity for displacement fields (C^0-HSDT). In this strategy, two other variables are added, and thence the first derivative of transverse displacements is only requested. From above reasons, a quadrilateral element with four nodes and seven degrees-of-freedom per node related to C^0-type of Reddy's third-order shear deformation theory and cell-based smoothed strains, is introduced for analyses of the FG-CNTRC plates. Based on the idea of using the high-order shear deformation theory through the C^0-type, the achieved results are given completely reliable without any regrettable phenomena. Furthermore, based on both classical and non-classical plate models suggested for small-scale structures [21, 22], the method proposed in this paper can be further developed in the future. By changing the material from CNTRC to GPLs or others [8], this plate model can be applied in the next research with a high expectation of stability and convergence.

This paper is organized as follows. The material properties of functionally graded carbon nanotube-reinforced composite (FG-CNTRC) plate, C^0-type of Reddy's third-order shear deformation theory, the finite element formulation for plate is briefly introduced in Section 2. To highlight the effectiveness of this element in analyzing the behaviors of FG-CNTRC plate structures, several numerical examples are thoroughly explored in Section 3. Finally, Section 4 has some logical conclusions.

Formulations

Material properties

Let's consider a FG-CNTRC plate with geometry as plotted in Figure 1. The top and bottom planes of plate are to be fully ceramic and metallic. The middle plane of structure is *xy*-plane, while the *z*-axis is depicted in Figure 1a.

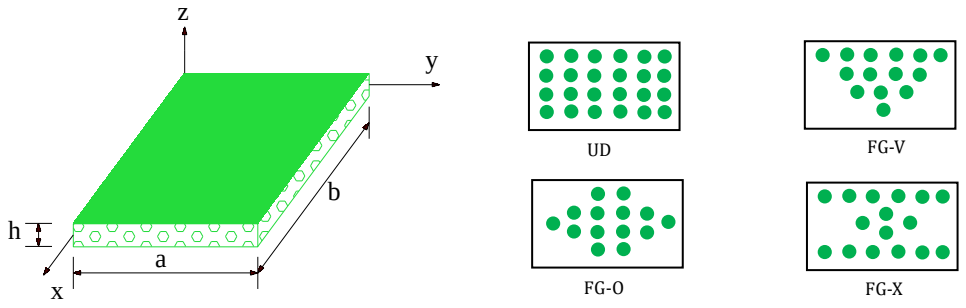

(a) (b)

Figure 1. (a) FG-CNTRC plate with (b) four types; UD, FG-V, FG-O & FG-X.

Four types, UD, FG-V, FG-O and FG-X, of CNTs are shown in Figure 1, which can be expressed as

$$V_C = \begin{cases} V_C^* & (\text{UD}) \\ (1+2z/h)V_C^* & (\text{FGV}) \\ 2(1-2|z|/h)V_C^* & (\text{FGO}) \\ 2(2|z|/h)V_C^* & (\text{FGX}) \end{cases} \tag{1}$$

with

$$V_C^* = \frac{\omega_C}{\omega_C + (\rho_C/\rho_m) - (\rho_C/\rho_m)\omega_C} \tag{2}$$

where ρ_C and ρ_m are the density of CNTs and the matrix, ω_C is the mass fraction of the CNTs. Based on the rule of extended mixtures, the material properties of CNTs are written as

$$E_{11} = \eta_1 V_C E_{11}^C + V_m E_m \tag{3}$$

$$\eta_2 / E_{22} = V_C / E_{22}^C + V_m / E_m \tag{4}$$

$$\eta_3 / G_{12} = V_C / G_{12}^C + V_m / \mathrm{G}_m \tag{5}$$

G_m and E_m recall the shear modulus and Young's modulus of the isotropic matrix; G_{12}^C and E_{11}^C, E_{22}^C are called the shear modulus and Young's modulus of CNTs, η_1, η_2 and η_3 are efficiency parameters of CNTs as introduced in Table 1. V_m and V_C are called the matrix and CNT volume fractions and note that $V_m + V_C = 1$. Similarly, Poisson's ratio ν_{12} is given as follows:

$$\nu_{12} = V_C^* \nu_{12}^C + V_m \nu_m \tag{6}$$

Table 1. The efficiency parameters of CNTs.

V_C^*	η_1	η_2	η_3
0.11	0.149	0.934	0.934
0.14	0.150	0.941	0.941
0.17	0.140	1.381	1.381

C^0-type higher-order shear deformation theory

Let Ξ be the domain associated with the middle plane of the plate. The displacement field can be described in terms of C^0-type with seven unknown variables as follows

$$u(x,y,z) = u_0 + \left(z + rz^3\right)\phi_x^b + rz^3\phi_x^s \tag{7}$$

$$v(x,y,z) = v_0 + \left(z + rz^3\right)\phi_y^b + rz^3\phi_y^s \qquad r = \frac{-4}{3h^2} \qquad -\frac{h}{2} \le z \le \frac{h}{2} \tag{8}$$

$$w(x,y,z) = w_0 \tag{9}$$

It can be seen that the above seven unknowns include three axial and transverse

displacements u_0, v_0, w_0, four rotations ϕ_x^b, ϕ_y^b and ϕ_x^s, ϕ_y^s due to the bending and shear effects. Based on the small strain assumptions, the strain-displacement relations can be provided

$$\begin{Bmatrix} \varepsilon_x \\ \varepsilon_y \\ \varepsilon_{xy} \\ \gamma_{yz} \\ \gamma_{xz} \end{Bmatrix} = \begin{Bmatrix} u_{0,x} + z\phi_{x,x}^b + z^3 r\left(\phi_{x,x}^s + \phi_{x,x}^b\right) \\ v_{0,y} + z\phi_{y,y}^b + z^3 r\left(\phi_{y,y}^s + \phi_{y,y}^b\right) \\ u_{0,y} + v_{0,x} + z\left(\phi_{x,y}^b + \phi_{y,x}^b\right) + z^3 r\left(\phi_{x,y}^s + \phi_{y,x}^s + \phi_{x,y}^b + \phi_{y,x}^b\right) \\ \left(\phi_y^b + w_{,y}\right) + z^2\left(3r\right)\left(\phi_y^s + \phi_y^b\right) \\ \left(\phi_x^b + w_{,x}\right) + z^2\left(3r\right)\left(\phi_x^s + \phi_x^b\right) \end{Bmatrix} \tag{10}$$

in matrix form

$$\begin{Bmatrix} \boldsymbol{\varepsilon} \\ \boldsymbol{\gamma} \end{Bmatrix} = \begin{Bmatrix} \boldsymbol{\varepsilon}^{(0)} \\ \boldsymbol{\gamma}^{(0)} \end{Bmatrix} + \mathrm{z}\begin{Bmatrix} \boldsymbol{\varepsilon}^{(1)} \\ \mathbf{0} \end{Bmatrix} + \mathrm{z}^2\begin{Bmatrix} \mathbf{0} \\ \boldsymbol{\gamma}^{(2)} \end{Bmatrix} + \mathrm{z}^3\begin{Bmatrix} \boldsymbol{\varepsilon}^{(3)} \\ \mathbf{0} \end{Bmatrix} \tag{11}$$

with

$$\boldsymbol{\varepsilon}^{(0)} = \begin{Bmatrix} u_{0,x} \\ v_{0,y} \\ u_{0,y} + v_{0,x} \end{Bmatrix}, \quad \boldsymbol{\varepsilon}^{(1)} = \begin{Bmatrix} \phi_{x,x}^b \\ \phi_{y,y}^b \\ \phi_{x,y}^b + \phi_{y,x}^b \end{Bmatrix}, \quad \boldsymbol{\varepsilon}^{(3)} = r\begin{Bmatrix} \phi_{x,x}^s + \phi_{x,x}^b \\ \phi_{y,y}^s + \phi_{y,y}^b \\ \phi_{x,y}^s + \phi_{x,y}^b + \phi_{y,x}^s + \phi_{y,x}^b \end{Bmatrix} \tag{12}$$

$$\boldsymbol{\gamma}^{(0)} = \begin{Bmatrix} \phi_y^b + w_{,y} \\ \phi_x^b + w_{,x} \end{Bmatrix}, \quad \boldsymbol{\gamma}^{(2)} = 3r\begin{Bmatrix} \phi_y^s + \phi_y^b \\ \phi_x^s + \phi_x^b \end{Bmatrix} \tag{13}$$

The constitutive equation is expressed

$$\boldsymbol{\sigma} = \mathbf{D}_m(\mathrm{z})(\boldsymbol{\varepsilon}^{(0)} + \mathrm{z}\boldsymbol{\varepsilon}^{(1)} + \mathrm{z}^3\boldsymbol{\varepsilon}^{(3)}) \tag{14}$$

$$\boldsymbol{\tau} = \mathbf{D}_s\left(z\right)\left(\boldsymbol{\gamma}^{(0)} + \mathrm{z}^2\boldsymbol{\gamma}^{(2)}\right) \tag{15}$$

in which

$$\boldsymbol{\sigma} = \begin{bmatrix} \sigma_x & \sigma_y & \sigma_{xy} \end{bmatrix}^{\mathrm{T}}, \quad \boldsymbol{\tau} = \begin{bmatrix} \tau_{yz} & \tau_{xz} \end{bmatrix}^{\mathrm{T}} \tag{16}$$

$$\mathbf{D}_m\left(z\right) = \frac{E\left(z\right)}{1-\nu^2\left(z\right)}\begin{bmatrix} 1 & \nu\left(z\right) & 0 \\ \nu\left(z\right) & 1 & 0 \\ 0 & 0 & \left(1-\nu\left(z\right)\right)/2 \end{bmatrix} \tag{17}$$

$$\mathbf{D}_s\left(z\right) = \frac{E\left(z\right)}{2\left(1+\nu\left(z\right)\right)}\begin{bmatrix} 1 & 0 \\ 0 & 1 \end{bmatrix} \tag{18}$$

The normal and shear forces, bending moments, higher-order values of moments and shear forces can be presented in matrix form as follows

$$\begin{Bmatrix}\mathbf{N}\\ \mathbf{M}\\ \mathbf{P}\\ \mathbf{Q}\\ \mathbf{R}\end{Bmatrix}=\begin{bmatrix}\mathbf{A} & \mathbf{B} & \mathbf{E} & \mathbf{0} & \mathbf{0}\\ \mathbf{B} & \mathbf{D} & \mathbf{F} & \mathbf{0} & \mathbf{0}\\ \mathbf{E} & \mathbf{F} & \mathbf{H} & \mathbf{0} & \mathbf{0}\\ \mathbf{0} & \mathbf{0} & \mathbf{0} & \hat{\mathbf{A}} & \hat{\mathbf{B}}\\ \mathbf{0} & \mathbf{0} & \mathbf{0} & \hat{\mathbf{B}} & \hat{\mathbf{D}}\end{bmatrix}\begin{Bmatrix}\boldsymbol{\varepsilon}^{(0)}\\ \boldsymbol{\varepsilon}^{(1)}\\ \boldsymbol{\varepsilon}^{(3)}\\ \boldsymbol{\gamma}^{(0)}\\ \boldsymbol{\gamma}^{(2)}\end{Bmatrix}=\begin{bmatrix}\mathbf{D}_1 & \mathbf{0}\\ \mathbf{0} & \mathbf{D}_2\end{bmatrix}\begin{Bmatrix}\boldsymbol{\varepsilon}^{(0)}\\ \boldsymbol{\varepsilon}^{(1)}\\ \boldsymbol{\varepsilon}^{(3)}\\ \boldsymbol{\gamma}^{(0)}\\ \boldsymbol{\gamma}^{(2)}\end{Bmatrix} \tag{19}$$

with

$$\left(\mathbf{A},\ \mathbf{B},\ \mathbf{D},\ \mathbf{E},\ \mathbf{F},\ \mathbf{H}\right)=\int_{-h/2}^{h/2}\left(1,\ z,\ z^2,\ z^3,\ z^4,\ z^6\right)\mathbf{D}_m^{i,j}(z)dz \tag{20}$$

$$\left(\hat{\mathbf{A}},\ \hat{\mathbf{B}},\ \hat{\mathbf{D}}\right)=\int_{-h/2}^{h/2}\left(1,\ z^2,\ z^4\right)\mathbf{D}_s^{i,j}(z)dz \tag{21}$$

For the static analysis, a weak form of plates can be given as:

$$\int_{\Xi}\delta\boldsymbol{\varepsilon}^T\mathbf{D}_1\boldsymbol{\varepsilon}d\Xi+\int_{\Xi}\delta\boldsymbol{\gamma}^T\mathbf{D}_2\boldsymbol{\gamma}d\Xi=\int_{\Xi}\delta wpd\Xi \tag{22}$$

where p is the distributed load in transverse direction. For the free vibration analysis, a weak form of plates can be derived from the following dynamic equation

$$\int_{\Xi}\delta\boldsymbol{\varepsilon}^T\mathbf{D}_1\boldsymbol{\varepsilon}d\Xi+\int_{\Xi}\delta\boldsymbol{\gamma}^T\mathbf{D}_2\boldsymbol{\gamma}d\Xi=\int_{\Xi}\delta\mathbf{u}^T\mathbf{m}\ddot{\mathbf{u}}d\Xi \tag{23}$$

Four-node quadrilateral element

Discretize the domain Ξ of plates into N_c finite elements and N_n is called the total number of nodes. The displacement field **u** of the standard FEM using the quadrilateral element with four nodes can be approximated by

$$\mathbf{u}=\sum_{i=1}^{N_n}\begin{bmatrix}N_i & 0 & 0 & 0 & 0 & 0 & 0\\ 0 & N_i & 0 & 0 & 0 & 0 & 0\\ 0 & 0 & N_i & 0 & 0 & 0 & 0\\ 0 & 0 & 0 & N_i & 0 & 0 & 0\\ 0 & 0 & 0 & 0 & N_i & 0 & 0\\ 0 & 0 & 0 & 0 & 0 & N_i & 0\\ 0 & 0 & 0 & 0 & 0 & 0 & N_i\end{bmatrix}\mathbf{q}_i \tag{24}$$

N_i is the shape function and $\mathbf{q}_i$ is the displacement vector of the nodal degrees of freedom of **u** associated to the i^{th} node. The strain can be rewritten

$$\boldsymbol{\varepsilon}=\sum_i\left(\mathbf{B}_1+\mathbf{B}_2+\mathbf{B}_3\right)\mathbf{q}_i \tag{25}$$

$$\boldsymbol{\gamma}=\sum_i\left(\mathbf{B}_4+\mathbf{B}_5\right)\mathbf{q}_i \tag{26}$$

in which

$$\mathbf{B}_1 = \begin{bmatrix} N_{i,x} & 0 & 0 & 0 & 0 & 0 & 0 \\ 0 & N_{i,y} & 0 & 0 & 0 & 0 & 0 \\ N_{i,y} & N_{i,x} & 0 & 0 & 0 & 0 & 0 \end{bmatrix} \tag{27}$$

$$\mathbf{B}_2 = \begin{bmatrix} 0 & 0 & 0 & 0 & 0 & N_{i,x} & 0 \\ 0 & 0 & 0 & 0 & 0 & 0 & N_{i,y} \\ 0 & 0 & 0 & 0 & 0 & N_{i,y} & N_{i,x} \end{bmatrix} \tag{28}$$

$$\mathbf{B}_3 = -\frac{4}{3h^2}\begin{bmatrix} 0 & 0 & 0 & N_{i,x} & 0 & N_{i,x} & 0 \\ 0 & 0 & 0 & 0 & N_{i,y} & 0 & N_{i,y} \\ 0 & 0 & 0 & N_{i,y} & N_{i,x} & N_{i,y} & N_{i,x} \end{bmatrix} \tag{29}$$

$$\mathbf{B}_4 = \begin{bmatrix} 0 & 0 & N_{i,y} & 0 & 0 & 0 & N_i \\ 0 & 0 & N_{i,x} & 0 & 0 & N_i & 0 \end{bmatrix} \tag{30}$$

$$\mathbf{B}_5 = -\frac{4}{h^2}\begin{bmatrix} 0 & 0 & 0 & 0 & N_i & 0 & N_i \\ 0 & 0 & 0 & N_i & 0 & N_i & 0 \end{bmatrix} \tag{31}$$

From the CS strategy, a quadrilateral element domain Ξ_C is further divided into $n_C = 2$ smoothing cells as Figure 2. By using the strain smoothing operation for each smoothing cell, the generalized strain field is presented

$$\bar{\boldsymbol{\varepsilon}}(x_C) = \int_{\Xi_C} \boldsymbol{\varepsilon}(x)\Phi\left(x - x_C\right)d\Xi \tag{32}$$

x_C is an arbitrary point to determine strains. The smoothed strain based on the divergence theorem can be achieved with

$$\bar{\mathbf{B}}_1 = \frac{1}{A_C}\sum_{m=1}^{4}\begin{bmatrix} N_i(x^G)n_x & 0 & 0 & 0 & 0 & 0 & 0 \\ 0 & N_i(x^G)n_y & 0 & 0 & 0 & 0 & 0 \\ N_i(x^G)n_y & N_i(x^G)n_x & 0 & 0 & 0 & 0 & 0 \end{bmatrix} l^C \tag{33}$$

$$\bar{\mathbf{B}}_2 = \frac{1}{A_C}\sum_{b=1}^{4}\begin{bmatrix} 0 & 0 & 0 & 0 & 0 & N_i(x^G)n_x & 0 \\ 0 & 0 & 0 & 0 & 0 & 0 & N_i(x^G)n_y \\ 0 & 0 & 0 & 0 & 0 & N_i(x^G)n_x & N_i(x^G)n_x \end{bmatrix} l^C \tag{34}$$

$$\bar{\mathbf{B}}_3 = -\frac{4}{3h^2}\sum_{b=1}^{4}\begin{bmatrix} 0 & 0 & 0 & N_i(x^G)n_x & 0 & N_i(x^G)n_x & 0 \\ 0 & 0 & 0 & 0 & N_i(x^G)n_y & 0 & N_i(x^G)n_y \\ 0 & 0 & 0 & N_i(x^G)n_y & N_i(x^G)n_x & N_i(x^G)n_y & N_i(x^G)n_x \end{bmatrix} l^C \tag{35}$$

by following [23, 24], in which x^G and l^C are the Gauss point and the length of each line segment of the boundary, n_x and n_y are two components of the unit outward vector normal to each edge, A_C is the area of the smoothing cell.

Completely similarly to literature [23–25], the element stiffness is then given

$$\bar{\mathbf{K}} = \sum_{C=1}^{n_C=2} (\bar{\mathbf{B}}_1^{\mathrm{T}} \bar{\mathbf{A}} \bar{\mathbf{B}}_1 + \bar{\mathbf{B}}_1^{\mathrm{T}} \bar{\mathbf{B}} \bar{\mathbf{B}}_2 + \bar{\mathbf{B}}_1^{\mathrm{T}} \bar{\mathbf{E}} \bar{\mathbf{B}}_3 + \bar{\mathbf{B}}_2^{\mathrm{T}} \bar{\mathbf{B}} \bar{\mathbf{B}}_1 + \bar{\mathbf{B}}_2^{\mathrm{T}} \bar{\mathbf{D}} \bar{\mathbf{B}}_2 + \bar{\mathbf{B}}_2^{\mathrm{T}} \bar{\mathbf{F}} \bar{\mathbf{B}}_3 + \bar{\mathbf{B}}_3^{\mathrm{T}} \bar{\mathbf{E}} \bar{\mathbf{B}}_1 + \bar{\mathbf{B}}_3^{\mathrm{T}} \bar{\mathbf{F}} \bar{\mathbf{B}}_2 + \bar{\mathbf{B}}_3^{\mathrm{T}} \bar{\mathbf{H}} \bar{\mathbf{B}}_3)$$
$$+ \int_{\Xi_C} (\mathbf{B}_4^{\mathrm{T}} \hat{\mathbf{A}} \mathbf{B}_4 + \mathbf{B}_4^{\mathrm{T}} \hat{\mathbf{B}} \mathbf{B}_5 + \mathbf{B}_5^{\mathrm{T}} \hat{\mathbf{B}} \mathbf{B}_4 + \mathbf{B}_5^{\mathrm{T}} \hat{\mathbf{D}} \mathbf{B}_5) d\Xi \tag{36}$$

For static analysis

$$\mathbf{Kq} = \mathbf{F} \tag{37}$$

with

$$\mathbf{F} = \int_{\Xi} \mathbf{p} \mathbf{N} d\Xi \tag{38}$$

For free vibration analysis

$$(\mathbf{K} - \omega^2 \mathbf{M})\mathbf{q} = \mathbf{0} \tag{39}$$

where

$$\mathbf{M} = \int_{\Xi} \mathbf{N}^T \mathbf{m} \mathbf{N} d\Xi \tag{40}$$

And **m**, by following the details in [26, 27], can be calculated from matrix **L** given as

$$\mathbf{L} = \begin{bmatrix} 1 & 0 & 0 & rz^3 & 0 & z + rz^3 & 0 \\ 0 & 1 & 0 & 0 & rz^3 & 0 & z + rz^3 \\ 0 & 0 & 1 & 0 & 0 & 0 & 0 \end{bmatrix} \tag{41}$$

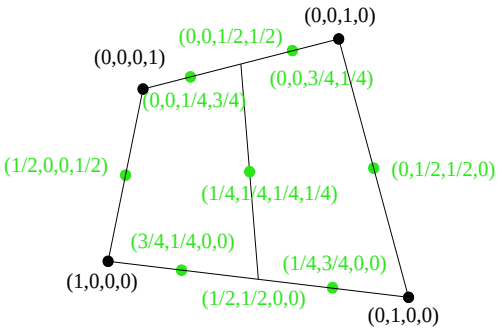

Figure 2. The subdivision of a quadrilateral element into $n_C = 2$ cells and the values of shape functions at nodes.

Numerical results

Verification

Firstly, the square plate as shown in Figure 3 with two kinds of boundary condition as simply supported (SSSS) and clamped (CCCC) under the change of the length to thickness ratio a/h = 10, 100, 1000, 10000 is analyzed. It is subjected to a uniformly distributed load q with material properties such as E = 1.092 MPa and ν = 0.3. More clearly, the boundary conditions are defined as follows:

Clamped (C): $u_o = v_o = w_o = \phi_x^s = \phi_x^b = \phi_y^s = \phi_y^b = 0$;

Simply supported (S): for left and right edges: $v_o = w_o = \phi_x^s = \phi_x^b = 0$

for upper and lower edges: $u_o = w_o = \phi_y^s = \phi_y^b = 0$

The normalized central deflection $w = (100Eh^3 w_c)/[12qa^4(1-\nu^2)]$ is presented in Table 2 and then compared with the exact solution in literature [28] as shown in Figure 4. Figure 4 shows the relative errors with 6 x 6, 8 x 8, 10 x 10, 12 x 12 and 14 x 14 meshes for (SSSS/CCCC) boundary condition and ratio *a/h* = 10, 100, 1000 and 10000. Based on changing the ratio a/h from 10 to 10000 and the results gradually converge, we can say that the proposed element overcomes the shear locking phenomenon.

The author continues to verify the reliability of the proposed element through various examples related to FG-CNTRC plate structures. Unless stated otherwise, material properties of matrix, PmPV, are expressed to be $E_m = 2.1Gpa$, $\nu_m = 0.34$ at the room temperature, and the reinforcements (10,10) SWCNTs are given by $E_{11}^C = 5.6466Tpa$, $E_{22}^C = 7.08Tpa$, $G_{12}^C = 1.9445Tpa$, $\nu_{12}^C = 0.175$. In addition, $G_{12} = G_{13} = G_{23}$ is assumed in this study.

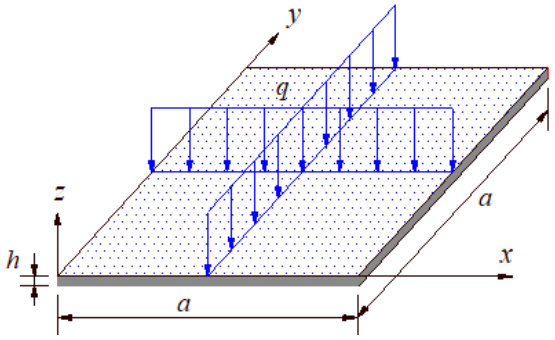

Figure 3. A square plate under uniformly distributed load.

Table 2. The normalized central deflection of the (SSSS/CCCC) square plate.

w^* (SSSS)					
Mesh	6 x 6	8 x 8	10 x 10	12 x 12	14 x 14
a/h = 10	0.428705	0.428053	0.427756	0.427607	0.427517
a/h = 100	0.406833	0.406661	0.406582	0.40654	0.406515
a/h = 1000	0.406614	0.406447	0.40637	0.406329	0.406305
a/h = 10000	0.406612	0.406445	0.406368	0.406327	0.406303
w^* (CCCC)					
Mesh	6 x 6	8 x 8	10 x 10	12 x 12	14 x 14
a/h = 10	0.149973	0.149973	0.150268	0.150302	0.150256
a/h = 100	0.126546	0.126640	0.126684	0.126716	0.126731
a/h = 1000	0.126300	0.126382	0.126433	0.126461	0.126479
a/h = 10000	0.126297	0.126379	0.126430	0.126459	0.126477

Bending analysis

The static bending of an FG-CNTRC plate under uniformly distributed load

$q = 10^5 \left(N / m^2 \right)$ with three values of CNTs volume fraction ($V_C^* = 0.11 / 0.14 / 0.17$) is studied in this example. Table 3 and Figure 5a compare the normalized central deflection of the (SSSS) FG-CNTRC square plates with the volume fraction of CNTs $V_C^* = 0.17$ and the length-to-thickness ratio *a/h* = 50 by five different methods, including commercial software package Ansys [19], CS-DSG3 [18], IGA [18], analytical [6] and the proposed element. Table 4 also presents the normalized central deflection for the FG-CNTRC square plates with the length-to-thickness ratio *a/h* = 20 and three values of the volume fraction of CNTs under two boundary conditions (SSSS) & (CCCC) in comparison with those of the CS-DSG3 [18] and the IGA's results [18]. It is observed that the present results match well with other solutions. It is also found that an increase in the volume fraction V_C^* of CNTs leads a decrease in the normalized central deflection of FG-CNTRC plates. With types FG-O and FG-X, the FG-CNTRC plate have the smallest and greatest stiffness because of the greatest and smallest deflections of them. Furthermore, Figure 5b illustrates the approximation among three methods' results for FG-CNTRC plate with $V_C^* = 0.11$.

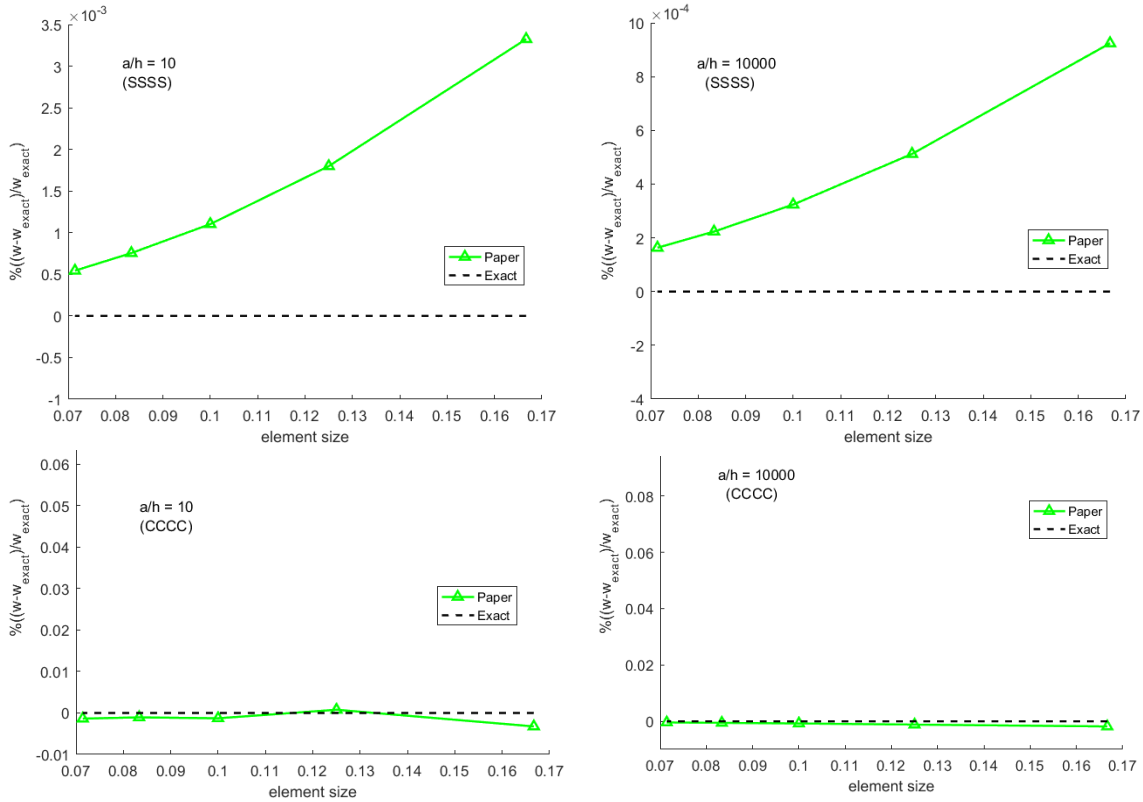

Figure 4. The relative error of the normalized deflection.

The effects of CNT volume fraction and length-to-thickness ratio *a/h* on the normalized central deflection for full types of FG-CNTRC square plates are presented in Table 5. The solutions of this element are compared with other results related to the commercial software package Ansys [19] as well as the standard FEM in [19]. It can be seen that three groups of results match very well. The slight difference in results may be

due to different approaches to solving the same problem. In some cases, the results obtained from the paper are closer to the analytical solutions than other results, for example, obtained from the IGA as shown in Table 3. Once again, it is found that the centric deflection of the plates is greatly influenced by the change in volume fraction of CNT. Specifically, this deflection will decrease to 30% when only 6% of the volume fraction of CNT is increased. Note that the central deflections of two types FG-V and FG-O plates are larger than those of two types UD and FG-X though all types of plates have the same mass fraction of the CNT.

Table 3. Comparison of normalized central deflection for the (SSSS) FG-CNTRC square plate with $V_C^* = 0.17$.

Types	Ansys	CS-DSG3	IGA	Analytical	Present
FG-X	0.5141	0.5144	0.5126	0.5156	0.5159
FG-O	1.4110	1.4153	1.4426	1.4120	1.4193
FG-V	1.0810	1.0834	1.1010	1.0820	1.0807
UD	0.7521	0.7524	0.7588	0.7523	0.7538

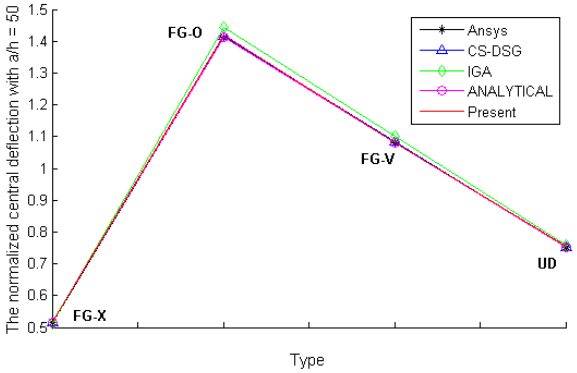

(a) SSSS, $V_C^* = 0.17$

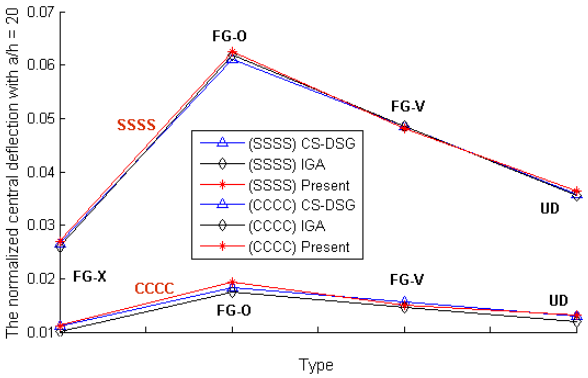

(b) SSSS, $V_C^* = 0.17$

Figure 5. The comparison of normalized central deflections in the FG-CNTRC plates under a uniform load.

By changing the distribution of reinforcements, the stiffness of plates can be affected, and this action is expected to get the desired stiffness of these structures in reality.

Furthermore, if these reinforcements are distributed on the bottom or top surface, the plates will achieve better stiffness than in other cases. This is an important comment to help the engineer determine a specific development direction with specific characteristics for each product created.

According to Figure 6, the normalized central axial stresses $\bar{\sigma}_{xx} = \sigma_{xx} h^2 / \left(|q| a^2 \right)$ of FG-CNTRC square plates along thickness direction with length-to-thickness ratio *a/h* = 50 and CNT volume fraction $V_C^* = 0.17$ based on the suggested element are collated with the results of [19]. Figure 6a under boundary condition (CCCC) as well as Figure 6b under boundary condition (SSSS) show that the paper's results match well with other results [19]. The central axial stress distribution in four types UD, FG-O, FG-V and FG-X CNTRC plates will differ as shown throughout the thickness. The axial stress equals zero at the bottom of FG-V CNTRC plate as well as the value of this quantity equals zero on both the top and bottom surface of the FG-O CNTRC plate.

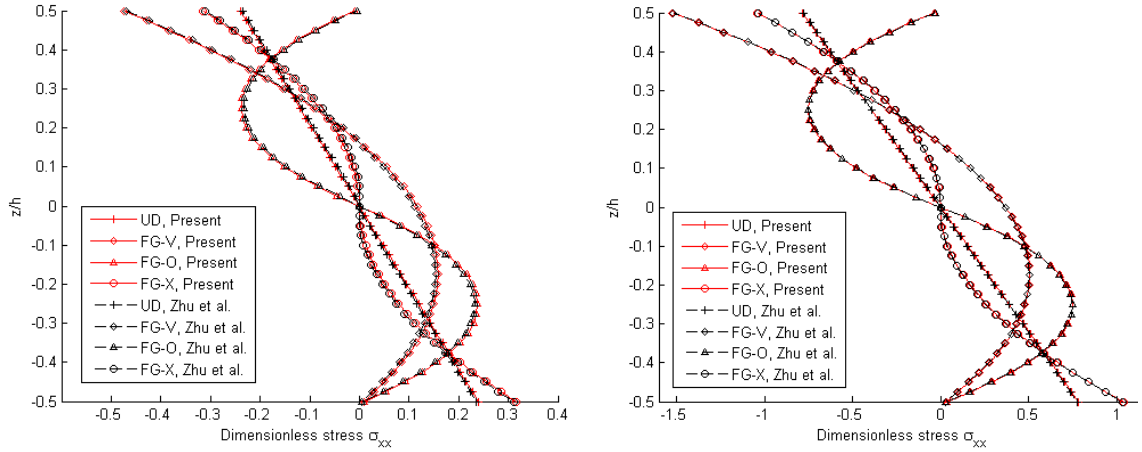

(a) *a/h* = 50, $V_C^* = 0.17$, (CCCC) (b) *a/h* = 50, $V_C^* = 0.17$, (SSSS)

Figure 6. The normalized central axial stresses in the FG-CNTRC plates under a uniform load.

Free vibration analysis

In this section, the efficiency and accuracy of this method for studying natural frequencies of FG-CNTRC plates are verified. The geometric and material properties of this structure are used similarly to those in above section. The normalized natural frequency is given $\bar{\omega} = \omega a^2 \sqrt{\rho_m / E_m} / h$. These values obtained by the proposed element and other methods are illustrated in Figure 7 and shown in Tables 6 & 7. It is observed that the present results match well with other solutions from [18, 19] for IGA and FEM strategies.

Finally, the normalized natural frequencies $\bar{\omega} = \omega a^2 \sqrt{\rho_m / D_m} / h$ of FG-CNTRC plates with central cutout as shown in Figure 8 are calculated, with D_m is called the flexural rigidity of a plate made from the polymeric matrix.

Tables 8 & 9 give the first three frequencies of CNTRC square plates with side-to-thickness ratio *a/h* = 20. They are connected with CCCC and SSSS plates, respectively.

The volume fraction of CNTs is taken as $V_C^* = 0.17$. In each case, the frequencies are calculated for three different perforation sizes and four different graded patterns of CNTs. It can be found that, similar to the case of plates without a cutout, in plates with a hole, FG-X type also has the highest fundamental frequency as well as FG-O type has the lowest. The effect of hole size on fundamental frequency is easily discernible. For example, in CCCC plates, the fundamental frequency of a plate increases when the hole size increases from $a_1/a = b_1/b$ = 0.1 to 0.3 and 0.5. Moreover, Tables 8 & 9 show that the approximation of results from two different ways like the presented method and the method related to Chebyshev polynomials as [20] can be achieved in this paper. Figure 9 describes the first six mode shapes of FG-CNTRC square plate with centric cutout a_1/a (b_1/b) = 0.5, length to thickness ratio a/h = 20 as well as CCCC boundary condition, respectively.

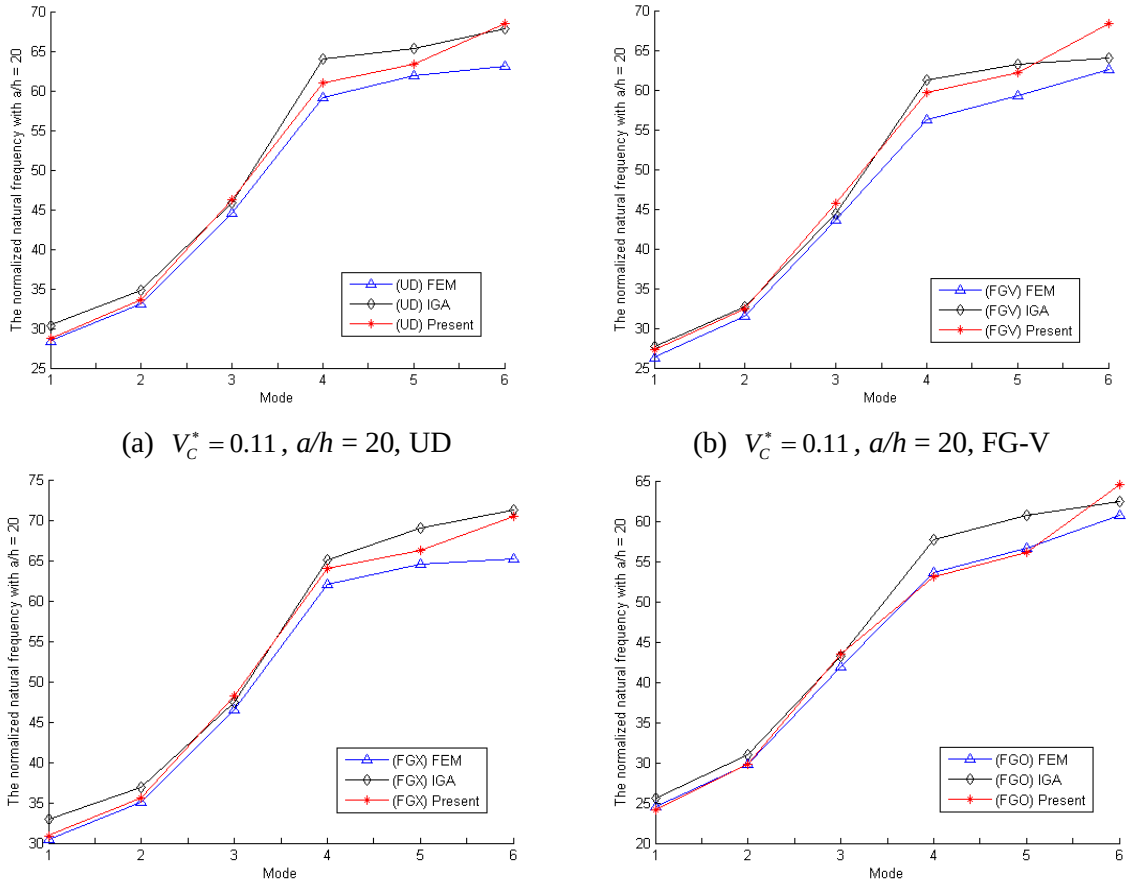

(a) $V_C^* = 0.11$, a/h = 20, UD

(b) $V_C^* = 0.11$, a/h = 20, FG-V

(c) $V_C^* = 0.11$, a/h = 20, FG-X

(d) $V_C^* = 0.11$, a/h = 20, FG-O

Figure 7. The comparison of normalized natural frequencies in the FG-CNTRC plates under CCCC boundary condition, $V_C^* = 0.11$, a/h = 20 & UD.

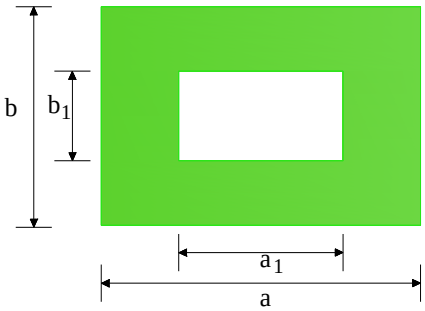

Figure 8. The FG-CNTRC plates with centric cutout.

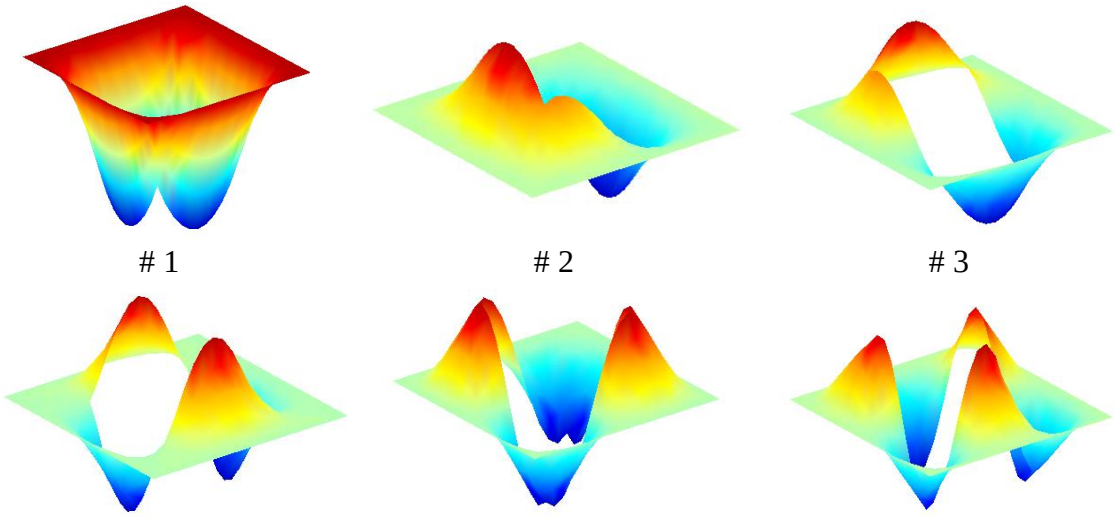

Figure 9. The first six mode shapes of (CCCC) FG-CNTRC square plate with a centric cutout, ratio a/h = 20 and a_1/a (b_1/b) = 0.5.

Conclusion

In this paper, the proposed element is given and successfully applied to bending and free vibration analysis of FG-CNTRC plate in the framework of the C^0-HSDT model and cell-based smoothed strains. This C^0-HSDT model supplies convergent results without shear correct factors. It is also noted that this element related to the C^0 type of HSDT only uses bilinear function approximations to analyze structures. The proposed element is shown to be free of shear locking and numerical results are presented in this paper approximately with other solutions from references.

Table 4. The comparison of normalized central deflection for the FG-CNTRC square plates with two boundary conditions (SSSS) & (CCCC) and three values of V_C^*

V_C^*	Types	SSSS			CCCC		
		CS-DSG3	IGA	Present	CS-DSG3	IGA	Present
0.11	FG-X	0.02664	0.02594	0.02701	0.01114	0.01016	0.01123
	FG-O	0.06116	0.06179	0.06254	0.01824	0.01747	0.01938
	FG-V	0.04846	0.04854	0.04802	0.01557	0.01472	0.01499
	UD	0.03589	0.03551	0.03635	0.01302	0.01205	0.01317
0.14	FG-X	0.02214	0.02140	0.02259	0.00999	0.00910	0.01014
	FG-O	0.05013	0.05040	0.05139	0.01565	0.01490	0.01663
	FG-V	0.03976	0.03962	0.03933	0.01352	0.01270	0.01295
	UD	0.02955	0.02900	0.02996	0.01150	0.01056	0.01162
0.17	FG-X	0.01715	0.01675	0.01755	0.00707	0.00749	0.00725
	FG-O	0.03995	0.04031	0.04065	0.01175	0.01131	0.01232
	FG-V	0.03153	0.03166	0.03126	0.00999	0.00951	0.00963
	UD	0.02324	0.02300	0.02353	0.00833	0.00873	0.00843

Table 5. The effects of length-to-thickness ratio *a/h* and volume fraction of CNT on the normalized central deflection for full types of FG-CNTRC square plates with two boundary conditions (SSSS) & (CCCC).

V_C^*	*a/h*	Type	SSSS			CCCC		
			Ansys	FEM	Present	Ansys	FEM	Present
0.11	10	FG-X	0.00318	0.00318	0.00315	0.00210	0.00211	0.00199
		FG-O	0.00522	0.00523	0.00544	0.00251	0.00251	0.00262
		FG-V	0.00446	0.00446	0.00426	0.00235	0.00235	0.00213
		UD	0.00374	0.00374	0.00373	0.00223	0.00223	0.00212
	20	FG-X	0.02703	0.02701	0.02701	0.01150	0.01150	0.01123
		FG-O	0.06136	0.06155	0.06254	0.01856	0.01860	0.01938
		FG-V	0.04876	0.04879	0.04802	0.01591	0.01593	0.01499
		UD	0.03629	0.03628	0.03635	0.01338	0.01339	0.01317
	50	FG-X	0.79150	0.79000	0.79176	0.19000	0.18940	0.18946
		FG-O	2.15000	2.15700	2.16510	0.47050	0.47190	0.47788
		FG-V	1.65200	1.65300	1.65016	0.36530	0.36490	0.35898
		UD	1.15500	1.15500	1.15720	0.26180	0.26180	0.26108
0.14	10	FG-X	0.00284	0.00284	0.00283	0.00198	0.00198	0.00187
		FG-O	0.00451	0.00453	0.00469	0.00231	0.00231	0.00238
		FG-V	0.00389	0.00389	0.00368	0.00218	0.00218	0.00198
		UD	0.00331	0.00330	0.00328	0.00209	0.00209	0.00196
	20	FG-X	0.02258	0.02256	0.02259	0.01035	0.01036	0.01014
		FG-O	0.05053	0.05070	0.05139	0.01600	0.01604	0.01663
		FG-V	0.04021	0.04025	0.03933	0.01388	0.01390	0.01295
		UD	0.03002	0.03001	0.02996	0.01188	0.01188	0.01162
	50	FG-X	0.62840	0.62710	0.62656	0.15660	0.15600	0.15709
		FG-O	1.73200	1.73800	1.73864	0.37970	0.38050	0.38386
		FG-V	1.32500	1.32600	1.31752	0.29580	0.29550	0.28858
		UD	0.91820	0.91750	0.91617	0.21310	0.21310	0.21235

…

…

0.17	10	FG-X	0.00201	0.00201	0.00203	0.00132	0.00132	0.00127
		FG-O	0.00337	0.00338	0.00347	0.00159	0.00160	0.00163
		FG-V	0.00286	0.00286	0.00274	0.00148	0.00149	0.00137
		UD	0.00239	0.00239	0.00239	0.00141	0.00141	0.00135
	20	FG-X	0.01738	0.01737	0.01755	0.00729	0.00729	0.00725
		FG-O	0.04007	0.04020	0.04065	0.01195	0.01198	0.01232
		FG-V	0.03171	0.03174	0.03126	0.01020	0.01021	0.00963
		UD	0.02349	0.02348	0.02353	0.00856	0.00856	0.00843
	50	FG-X	0.51410	0.51320	0.51590	0.12270	0.12230	0.12319
		FG-O	1.41100	1.41600	1.41929	0.30790	0.30850	0.31129
		FG-V	1.08100	1.08200	1.08066	0.23860	0.23840	0.23481
		UD	0.75210	0.75150	0.75380	0.16990	0.16980	0.16945

Table 6. The first six frequencies of FG-CNTRC square plates with $V_C^* = 0.11$, CCCC boundary condition and ratio *a/h* = 20

Mode	UD			FG-V			FG-X			FG-O		
	FEM	IGA	Present	FEM	IGA	Present	FEM	IGA	Present	FEM	IGA	Present
1	28.400	30.391	28.770	26.304	27.709	27.244	30.421	32.901	30.916	24.486	25.592	24.171
2	33.114	34.828	33.582	31.496	32.651	32.465	35.036	36.966	35.584	29.795	30.931	29.781
3	44.559	45.827	46.295	43.589	44.377	45.749	46.480	47.379	48.220	41.895	43.202	43.444
4	59.198	64.011	61.003	56.249	61.232	59.705	61.980	65.023	64.067	53.557	57.724	53.149
5	61.851	65.386	63.311	59.221	63.176	62.230	64.562	68.983	66.263	56.617	60.742	56.099
6	63.043	67.826	68.440	62.608	63.996	68.375	65.174	71.200	70.488	60.719	62.455	64.523

Table 7. The first six frequencies of FG-CNTRC square plates with $V_C^* = 0.14 \& 0.17$, CCCC boundary condition and *a/h* = 20

V_C^*	Mode	UD			FG-V			FG-X			FG-O		
		FEM	IGA	Present	FEM	IGA	Present	FEM	IGA	Present	FEM	IGA	Present
0.14	1	29.911	32.268	30.369	27.926	29.627	29.041	31.857	34.639	32.317	26.127	27.517	25.846
	2	34.516	36.585	35.052	32.976	34.401	34.087	36.487	38.623	37.004	31.186	32.661	31.179
	3	45.898	47.472	47.686	44.989	45.977	47.252	48.087	48.967	49.817	43.034	44.770	44.579
	4	61.628	65.710	63.665	58.951	64.566	62.754	64.334	66.682	66.382	56.403	61.233	56.202
	5	64.199	68.494	65.869	61.816	64.816	65.142	66.912	71.812	68.569	59.277	64.075	58.930
	6	64.496	70.862	69.982	64.135	67.218	70.028	67.148	73.977	72.507	61.793	64.118	66.996
0.17	1	35.316	37.741	35.764	32.686	34.300	33.819	38.026	40.936	38.323	30.325	31.644	30.120
	2	41.253	43.336	41.826	39.279	40.563	40.467	44.105	46.048	44.482	36.848	38.419	36.994
	3	55.627	57.163	57.795	54.560	55.344	57.272	58.927	59.115	60.876	51.757	53.898	53.825
	4	73.769	79.971	75.986	70.149	76.015	74.391	77.640	81.214	79.443	66.657	71.569	66.706
	5	77.109	81.390	78.898	73.926	78.956	77.617	81.040	85.988	82.400	70.401	75.416	70.277
	6	78.801	84.469	85.552	78.522	79.526	85.785	82.932	88.769	89.382	75.018	78.100	80.551

Table 8. The comparison of the first three frequencies for FG-CNTRC square plates with $V_C^* = 0.17$, CCCC boundary condition, ratio *a/h* = 20 and centric cutout.

a_1/a (b_1/b)	Type	Mode 1		Mode 2		Mode 3	
		Ritz-Chebyshev	Present	Ritz-Chebyshev	Present	Ritz-Chebyshev	Present
0.1	UD	105.467	105.585	127.453	127.678	178.296	179.315
	FG-X	114.074	113.991	136.167	136.421	188.906	188.004
	FG-O	90.332	90.879	114.938	115.035	167.119	167.645
	FG-V	97.556	98.004	122.224	122.829	175.891	176.218
0.3	UD	120.444	120.865	126.966	126.526	169.807	170.115
	FG-X	130.605	130.211	136.397	136.713	181.185	181.924
	FG-O	102.708	102.908	112.474	112.809	150.962	151.437
	FG-V	111.198	111.434	120.288	120.944	160.606	159.992
0.5	UD	144.342	144.712	145.095	145.555	220.784	221.044
	FG-X	155.389	155.837	156.225	156.607	233.783	232.898
	FG-O	129.162	128.989	129.991	130.130	196.190	196.665
	FG-V	137.889	138.012	138.757	139.096	208.316	209.034

Table 9. The comparison of the first three frequencies for FG-CNTRC square plates with $V_C^* = 0.17$, SSSS boundary condition, ratio *a/h* = 20 and centric cutout.

a_1/a (b_1/b)	Type	Mode 1		Mode 2		Mode 3	
		Ritz-Chebyshev	Present	Ritz-Chebyshev	Present	Ritz-Chebyshev	Present
0.1	UD	62.802	62.978	83.185	84.284	131.883	132.424
	FG-X	72.441	73.112	92.145	92.675	141.588	142.027
	FG-O	49.029	50.104	72.410	73.087	123.092	123.876
	FG-V	54.824	54.067	78.193	78.429	130.215	131.421
0.3	UD	52.823	52.333	78.351	78.878	111.674	112.013
	FG-X	60.572	61.745	87.199	87.645	119.193	120.469
	FG-O	41.986	42.412	67.447	68.198	100.770	101.048
	FG-V	46.742	47.527	73.082	73.917	107.283	107.954
0.5	UD	49.770	50.049	72.212	71.969	75.643	75.111
	FG-X	56.207	55.998	80.572	81.006	80.891	81.233
	FG-O	40.916	41.213	31.273	32.107	69.656	70.265
	FG-V	45.090	45.789	66.758	67.148	73.997	74.043

References

[1] X.-M. Liu *et al.* Carbon nanotube (CNT)-based composites as electrode material for rechargeable Li-ion batteries: A review. Composites Science and Technology, 72(2):121-144, 2012. https://doi.org/10.1016/j.compscitech.2011.11.019

[2] A. V. Herrera-Herrera, M. Á. González-Curbelo, J. Hernández-Borges, and M. Á. Rodríguez-Delgado. Carbon nanotubes applications in separation science: A review. Analytica Chimica Acta, 734:1-30, 2012. https://doi.org/10.1016/j.aca.2012.04.035

[3] S. K. Soni, B. Thomas, and V. R. Kar. A Comprehensive Review on CNTs and CNT-Reinforced Composites: Syntheses, Characteristics and Applications. Materials Today Communications, 25:p101546, 2020. https://doi.org/10.1016/j.mtcomm.2020.101546

[4] X. Zhou *et al.* Design, preparation and measurement of protein/CNTs hybrids: A concise review. Journal of Materials Science & Technology, 46:74-87, 2020. https://doi.org/10.1016/j.jmst.2020.01.008

[5] K. M. Liew, Z. X. Lei, and L. W. Zhang. Mechanical analysis of functionally graded carbon nanotube reinforced composites: A review. Composite Structures, 120:90-97, 2015. https://doi.org/10.1016/j.compstruct.2014.09.041

[6] A. Alibeigloo and A. Emtehani. Static and free vibration analyses of carbon nanotube-reinforced composite plate using differential quadrature method. Meccanica, 50(1):61-76, 2015. https://doi.org/10.1007/s11012-014-0050-7

[7] M. H. Majidi, M. Azadi, and H. Fahham. Vibration analysis of cantilever FG-CNTRC trapezoidal plates. Journal of the Brazilian Society of Mechanical Sciences and Engineering, 42(3):p.118, 2020. https://doi.org/10.1007/s40430-019-2151-7

[8] H. L. Ton-That, H. Nguyen-Van, and T. Chau-Dinh. A novel quadrilateral element for analysis of functionally graded porous plates/shells reinforced by graphene platelets. Archive of Applied Mechanics, 91(6):2435-2466, 2021. https://doi.org/10.1007/s00419-021-01893-6

[9] H. L. Ton-That and H. Nguyen-Van. A Combined Strain Element in Static, Frequency and Buckling Analyses of Laminated Composite Plates and Shells. Periodica Polytechnica Civil Engineering, 65(1):56-71, 2021. https://doi.org/10.3311/PPci.16809

[10] H. L. Ton-That. A Combined Strain Element to Functionally Graded Structures in Thermal Environment. Acta Polytechnica, 60(6):528-539, 2020. https://doi.org/10.14311/AP.2020.60.0528

[11] A. K. Singh and A. Bhar. Isogeometric FE analysis of laminated composite and functionally graded CNT reinforced composite plates using HSDT. Materials Today: Proceedings, 26:891-896, 2020. https://doi.org/10.1016/j.matpr.2020.01.129

[12] P. Xiang, Q. Xia, L. Z. Jiang, L. Peng, J. W. Yan, and X. Liu. Free vibration analysis of FG-CNTRC conical shell panels using the kernel particle Ritz element-free method. Composite Structures, 255:p.112987, 2021. https://doi.org/10.1016/j.compstruct.2020.112987

[13] A. Farzam and B. Hassani. Thermal and mechanical buckling analysis of FG carbon nanotube reinforced composite plates using modified couple stress theory and isogeometric approach. Composite Structures, 206:774-790, 2018. https://doi.org/10.1016/j.compstruct.2018.08.030

[14] T. Zhou and Y. Song. Three-dimensional nonlinear bending analysis of FG-CNTs reinforced composite plates using the element-free Galerkin method based on the S-R decomposition theorem. Composite Structures, 207:519-530, 2019. https://doi.org/10.1016/j.compstruct.2018.09.026

[15] Z. X. Lei, K. M. Liew, and J. L. Yu. Large deflection analysis of functionally graded carbon nanotube-reinforced composite plates by the element-free kp-Ritz method. Computer Methods in Applied Mechanics and Engineering, 256:189-199, 2013. https://doi.org/10.1016/j.cma.2012.12.007

[16] R. Ansari, J. Torabi, and M. F. Shojaei. Vibrational analysis of functionally graded carbon nanotube-reinforced composite spherical shells resting on elastic foundation using the variational differential quadrature method. European Journal of Mechanics - A/Solids, 60:166-182, 2016. https://doi.org/10.1016/j.euromechsol.2016.07.003

[17] T. Chau-Dinh, T. K. Nguyen, H. Nguyen-Van, and H. L. Ton-That. A MITC3+ element improved by edge-based smoothed strains for analyses of laminated composite plates using the higher-order shear deformation theory. Acta Mechanica, 232(2):389-422, 2021. https://doi.org/10.1007/s00707-020-02834-0

[18] T. Truong-Thi, T. Vo-Duy, V. Ho-Huu, and T. Nguyen-Thoi. Static and Free Vibration Analyses of Functionally Graded Carbon Nanotube Reinforced Composite Plates using CS-DSG3. International Journal of Computational Methods, 17(3): p.1850133, 2018. https://doi.org/10.1142/S0219876218501335

[19] P. Zhu, Z. X. Lei, and K. M. Liew. Static and free vibration analyses of carbon nanotube-reinforced composite plates using finite element method with first order shear deformation plate theory. Composite Structures, 94(4):1450-1460, 2012. https://doi.org/10.1016/j.compstruct.2011.11.010

[20] M. Mostafa and K. Yaser. Free vibration of functionally graded carbon-nanotube-reinforced composite plates with cutout. Beilstein Journal of Nanotechnology, 7:511-523, 2016. https://doi.org/10.3762/bjnano.7.45

[21] M. Mousavi Khoram, M. Hosseini, and M. Shishesaz. A concise review of nano-plates. Journal of Computational Applied Mechanics, 50(2):420-429, 2019. https://dx.doi.org/10.22059/jcamech.2019.293625.459

[22] H.-T. Thai, T. P. Vo, T.-K. Nguyen, and S.-E. Kim. A review of continuum mechanics models for size-dependent analysis of beams and plates. Composite Structures, 177:196-219, 2017. https://doi.org/10.1016/j.compstruct.2017.06.040

[23] H. H. Tai, N. V. Hieu, and V. D. Thang. Bending and free vibration behaviors of composite plates using the C0 -HSDT based four-node element with in-plane rotations. Journal of Science and Technology in Civil Engineering NUCE, 14(1):42-53, 2020. https://doi.org/10.31814/stce.nuce2020-14(1)-04

[24] L. T. That-Hoang, H. Nguyen-Van, T. Chau-Dinh, and C. Huynh-Van. Enhancement to four-node quadrilateral plate elements by using cell-based smoothed strains and higher-order shear deformation theory for nonlinear analysis of composite structures. Journal of Sandwich Structures & Materials,

22(7):2302-2329, 2020. https://doi.org/10.1177/1099636218797982
[25] H. L. Ton-That. A new C0 third-order shear deformation theory for the nonlinear free vibration analysis of stiffened functionally graded plates. Facta Universitatis, Series: Mechanical Engineering, 19(2):285-305, 2021. https://doi.org/10.22190/FUME200629040T
[26] T. Q. Bui *et al.* On the high temperature mechanical behaviors analysis of heated functionally graded plates using FEM and a new third-order shear deformation plate theory. Composites Part B: Engineering, 92:218-241, 2016. https://doi.org/10.1016/j.compositesb.2016.02.048
[27] H. L. Ton-That. Finite Element Analysis of Functionally Graded Skew Plates in Thermal Environment based on the New Third-order Shear Deformation Theory. Journal of Applied and Computational Mechanics, 6(4):1044-1057, 2020. https://dx.doi.org/10.22055/jacm.2019.31508.1881
[28] R. L. Taylor and F. Auricchio. Linked interpolation for Reissner-Mindlin plate elements: Part II—A simple triangle. International Journal for Numerical Methods in Engineering, 36(18):3057-3066, 1993. https://doi.org/10.1002/nme.1620361803

Lan Hoang Ton-That
Department of Civil Engineering
Ho Chi Minh City University of Architecture, Vietnam
lan.tonthathoang@uah.edu.vn